energy&fuels

pubs.acs.org/EF

Article

Waste Hemp Hurd as a Sustainable Precursor for Affordable and High-Rate Hard Carbon-Based Anodes in Sodium-Ion Batteries

Daniel Antorán, Darío Alvira, M. Eser Peker, Hugo Malón, Silvia Irusta, Víctor Sebastián, and Joan J. Manyà*

Cite This: *Energy Fuels* 2023, 37, 9650−9661

Read Online

ACCESS | Metrics & More | Article Recommendations | Supporting Information

ABSTRACT: The present study reports the promising potential of waste hemp-hurd-derived carbons as anodes in sodium-ion batteries (SIBs). Carbons were produced through an easily scalable process consisting of pyrolysis of raw biomass at 500 °C followed by mild chemical activation of the resulting char through wet impregnation with K_2CO_3 and subsequent heating of the solid phase (after filtration and drying) up to 700 or 800 °C under nitrogen. The best electrochemical performance was observed for the hard carbon activated at a char-K_2CO_3 mass ratio of 1:4 and heated up to 800 °C, which exhibited an excellent initial coulombic efficiency (73%) and achieved reversible charge capacities of 267 and 79 mAh g^{-1} at 0.03 and 1 A g^{-1}, respectively. This material also exhibited an impressive cyclic stability and rate capability, with a capacity retention of 96% after 300 cycles at a current density of 2 A g^{-1}. This more than satisfactory performance could be related to the textural and structural features of the hard carbon, which include moderate interconnected microporosity (with pore sizes below 1 nm), an appropriate concentration of defects in the carbon structure, relatively large interplanar distances, and a certain number of closed pores.

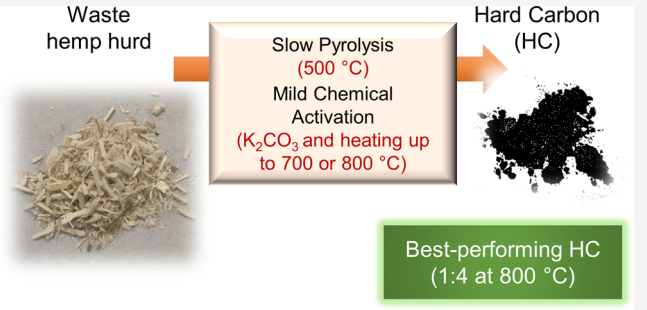

INTRODUCTION

Batteries are a growing source of interest as the world moves toward a more sustainable energy scenario. In the last 30 years, considerable progress was made in the research of new electrochemical energy storage (EES) systems, lithium-ion batteries (LIBs) being the most implemented technology since its commercialization by Sony in 1990s, owing to their high energy density and long cycle-life.[1] However, the supply of raw materials for LIBs (e.g., lithium, cobalt, and natural graphite) may become strained in the future, due to the limited availability of such materials as well as geopolitical factors.[2,3] In addition, the need for stabilizing the electricity system from intermittent renewable sources in the carbon-neutral future requires a massive expansion of energy storage capacity,[4] which has to be materialized using alternative post-lithium EES technologies based on more abundant and sustainable raw materials.

Among the different alternatives to LIBs, sodium-ion batteries (SIBs) have received growing attention by the research community, since sodium is more abundant, widely distributed, and cheaper than lithium. Both elements have similar standard reduction potentials (−3.04 V vs SHE for Li^+/Li and −2.71 V vs SHE for Na^+/Na) and tend to lose an electron from the outer energy level. In spite of these shared features, developing SIBs still requires intensive research efforts aimed at, among other things, finding high-performance electrode materials.[5] For the anode (or negative electrode), where graphite (which is extensively used in commercial LIBs) is not suitable due to thermodynamic issues,[6] hard carbons (HCs) have been widely considered as promising candidates since they can provide a number of active sites to reversibly store sodium ions. This is because HCs keep highly disordered structures with randomly oriented pseudographitic domains, some residual heteroatoms, and larger interlayer spacing (in comparison with graphitic carbons). Furthermore, lignocellulosic biomass can be used as a precursor of HCs, resulting in attractive valorization routes for biomass waste streams, on the one side, and low-cost and abundant raw materials for post-lithium EES systems, on the other. The resulting biomass-derived HCs can inherit or develop further appropriate porous nanostructures, such as 3D honeycomb-like networks, that can shorten the diffusion paths of Na ions and provide a number of ion buffering reservoirs.[7] Nevertheless, fine tuning the textural and structural features of biomass-derived carbons toward

Received: March 27, 2023
Revised: May 27, 2023
Published: June 8, 2023

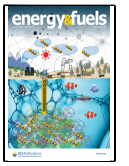

https://doi.org/10.1021/acs.energyfuels.3c01040
Energy Fuels 2023, 37, 9650−9661

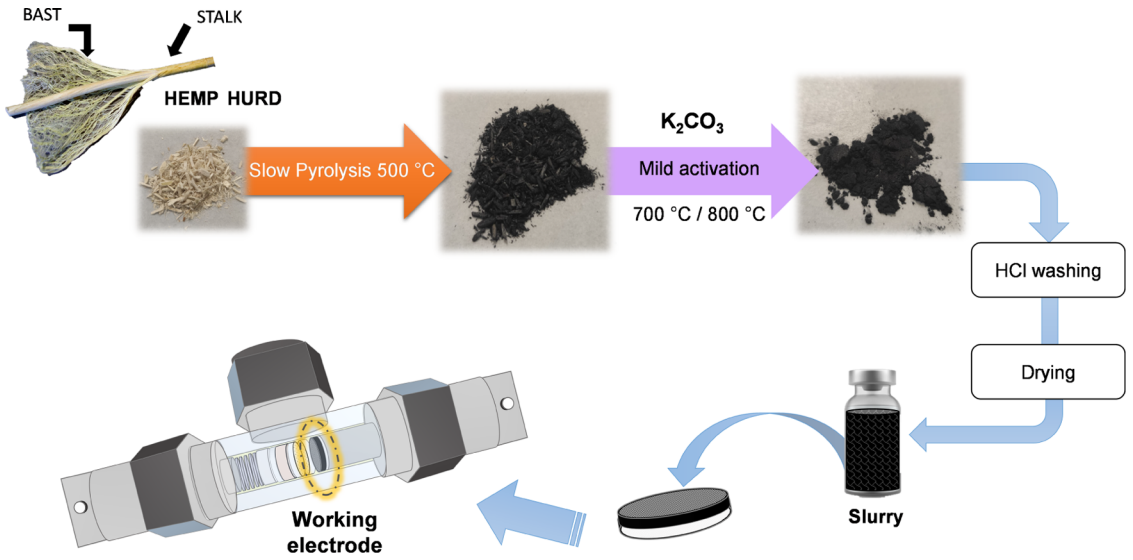

Figure 1. Schematic representation of the procedure adopted to synthesize HC-based electrode materials.

active anode materials with superior performance is still a big challenge.[8]

Activation processes could be useful to regulate the pore size distribution of the resulting HCs. In this sense, a hierarchical porous structure (containing mainly narrow micropores and certain large micropore and mesopore volumes) could significantly enhance charge transfer kinetics.[9,10] However, excessively large surface areas usually lead to the formation of thick solid electrolyte interphases (SEIs), resulting in low initial coulombic efficiency (ICE) values. As an interesting example in this regard, Hong et al. reported an impressive rate capability (95 and 71 mAh g^{-1} at 2 and 5 A g^{-1}, respectively) for pomelo peel-derived carbons produced through chemical activation with H_3PO_4;[11] however, the authors reported an ICE of only 27%, disabling this electrode material for real applications.

Activated carbons are commonly synthesized via physical (using an oxidative gas under controlled degrees of burnout) or chemical processes.[12] In the latter case, the raw material is impregnated with a chemical agent and subsequently heated under an inert atmosphere.[13] KOH is the most frequently used chemical since large specific surface areas and total pore volumes can be obtained.[14,15] However, using KOH at an industrially relevant scale is challenging due to corrosion issues. Alternatively, K_2CO_3 can be used as a chemical agent toward a mild activation approach,[16−18] which may result in moderate porosity developments.[19−22]

Waste hemp hurd (WHH), which is the lignocellulosic residue from industrial hemp stalks used for the production of fibers, was selected as biomass feedstock in the preset study. It accounts for ∼50 wt % of the whole plant biomass. Since there is a growing interest for hemp cultivation, due to the related environmental benefits, one can expect a growing production of WHH worldwide. Only in the EU, hemp production grew by 64% from 2015 to 2019.[23] Although the use of WHH as a precursor of electrode materials for LIBs and supercapacitors has already been investigated (see, for instance, the studies by Um et al.[24] and Wang et al.[25]), its suitability as a raw material for anodes in SIBs has been scarcely assessed. However, the study by Wang et al.,[26] who reported a promising reversible specific capacity of 256 mAh g^{-1} (at 0.374 A g^{-1}) for a surface-reconstructed (via high current charging and discharging pretreatment) WHH-derived hard carbon, should be highlighted.

With all of the above in mind, the specific aim of the present study is to produce HCs from WHH via mild chemical activation with K_2CO_3 and subsequent annealing at moderate temperature (i.e., 700 and 800 °C) as a fully scalable, environmentally benign, and economically sound production process. As outlined in the following sections, the best HC tested exhibited an electrochemical performance—in terms of specific capacity, cycling stability, and rate capability—that was comparable to that reported for other biomass-derived HCs, which were synthesized at higher carbonization temperatures and/or using more expensive and/or corrosive chemical agents. More insistingly, the best-performing material reported here exhibited an ICE of 73%, which was certainly high for biomass-derived carbon.

EXPERIMENTAL SECTION

Synthesis of WHH-Derived Hard Carbons. Waste hemp (*Cannabis sativa* L.) hurd from Narlisaray (Black Sea region of Turkey) was used as biomass feedstock. The as-received WHH was characterized in terms of proximate and elemental analyses, contents of inorganic species in ash by ICP-MS, and determination of the contents of main biomass constituents (i.e., hemicelluloses, cellulose, and lignin) using a method reported by Rodríguez-Correa et al.[27] Biomass (previously sieved to 5 mm in length) was first pyrolyzed at atmospheric pressure, an average heating rate of 5 °C min^{-1}, and a highest temperature of 500 °C. For this purpose, a bench-scale fixed-bed reactor, working under a steady pure nitrogen flow (leading to a gas residence time of 100 s at 500 °C), was used (see more details on the pyrolysis device in previous works[28,29]). The resulting WHH-based char was then chemically activated with K_2CO_3 through wet impregnation at char-activating agent mass ratios of 1:1, 1:2, and 1:4. The resulting mixtures were stirred for 2 h at 50 °C, filtered, and dried overnight at 120 °C and finally heated under nitrogen at a heating rate of 10 °C min^{-1} until 1 h after the target highest carbonization temperature (700 or 800 °C) was reached. A tubular reactor (made of EN 2.4816 alloy, 600 mm long and 28 mm ID), placed inside a vertical tubular furnace (model EVA 12/300 from Carbolite Gero), was employed. The gas hourly space velocity (GHSV) was fixed at 7000 h^{-1}, considering a void factor of 0.5. The resulting material was cooled to room temperature and then washed with HCl aqueous solution (2 mol dm^{-3}) to remove the excess of inorganic impurities

https://doi.org/10.1021/acs.energyfuels.3c01040
Energy Fuels 2023, 37, 9650−9661

and unreacted K_2CO_3. Finally, activated carbons were rinsed with distilled water until neutral pH, dried at 110 °C overnight, and ground and sieved to particle sizes below 90 μm. The produced hard carbons were named as HC−T−R, where T is the activation temperature and R refers to the impregnation mass ratio. Figure 1 graphically summarizes the procedure adopted for the synthesis of WHH-derived HCs.

Physicochemical Characterization. The microporosity of the produced HCs was assessed from both N_2 and CO_2 adsorption isotherms at −196 and 0 °C, respectively, which were acquired using an Autosorb-iQ-XR2 analyzer from Quantachrome Instruments. Specific surface areas (S_{BET}) were calculated by the Brunauer−Emmett−Teller equation. Micropore and mesopore volumes were estimated from N_2 adsorption data, whereas the ultramicropore volume (for pore sizes below 0.7 nm) was calculated from CO_2 adsorption data. NLDFT models (for slit pore geometry) in QuadraWin 6.0 software were adopted.

The morphology and elemental composition on the surface of the synthesized HCs were analyzed using SEM-EDX (Inspect F50A microscope from FEI). HRTEM (Titan microscope from FEI, with a SuperTwin objective lens and a CETCOR Cs-objective, allowing a point-to-point resolution of 0.08 nm) images were also obtained to investigate the structural features of HCs. Digitalmicrograph software was used to measure interlayer distances from HRTEM images. Structural characterization was further assessed by X-ray diffraction (Empyrean instrument from Malvern Panalytical at a wavelength of 0.154 nm) and Raman spectroscopy (alpha 300 microscope from Witec with samples excited at 532 nm). For the latter technique, each HC was analyzed on at least three different surface locations for a depth of 3 μm. XPS (Axis Supra spectrometer from Katros, using monochromatic Al Kα radiation source running at 1486 eV) was also applied to identify the oxygen- and nitrogen-containing functional groups on the surface from deconvolution of C 1s and N 1s regions. Peaks were fitted using Gaussian−Lorentzian sum functions after Shirley-type background subtraction in CasaXPS software.

Electrochemical Measurements. Working electrodes were prepared by mixing the WHH-derived HC with acetylene black (as conductive agent) and styrene−butadiene rubber (SBR) and carboxymethyl cellulose (CMC) (as binder compounds) at a mass ratio of 80:10:5:5. A homogeneous slurry was obtained by adding DI water with vortex agitation and magnetic stirring. The resulting mixture was uniformly coated on a high-purity aluminum sheet (current collector) using a baker applicator to obtain a 100-μm-thickness film. The resulting composite electrode was then punched (12 mm diameter) and dried under vacuum at 120 °C overnight. The final mass loading of the electrodes was 1.97 ± 0.37 mg cm^{-2}. Tailored t-type Swagelok half-cells were used to measure the electrochemical performance of WHH-based HCs (working electrode, WE) under a constant pressure of 0.2 N mm^{-2} (see Figure S1). The plugs were made of EN 1.4044 stainless steel, and a high-density polyethylene tube was used to host the electrodes. The cells were assembled in an argon-filled glovebox, with O_2 and H_2O contents less than 0.5 ppm. A sodium metal disc (12 mm diameter) was used as the counter electrode (CE) and reference electrode (RE) in two-electrode setups, while an additional disc of metal sodium (5 mm diameter) was used as the RE in the three-electrode cell (see Figure S1). To separate the electrode compartments, a glass fiber filter was used. The electrolyte (60 μL) was composed of a solution of NaTFSI (1 mol dm^{-3}) in a mixture (1:1 vol) of dimethyl carbonate and ethylene carbonate as the solvent.

Electrochemical measurements were performed using a potentiostat-galvanostat (model SP-200 from Bio-Logic) at room temperature. Galvanostatic discharge/charge (GCD) measurements were conducted within a potential window of 0.01−2.5 V (vs Na/Na$^+$), whereas cyclic voltammetry (CV) curves were obtained at a scan rate of 0.1 mV s^{-1} within the same voltage window. Galvanostatic intermittent titration technique (GITT) measurements were also conducted at a constant current density of 0.03 A g^{-1}, a pulse time of 20 min, and relaxation periods of 1 h at an open circuit.

RESULTS AND DISCUSSION

Properties of Raw WHH. Table 1 reports the results from proximate, elemental, inorganic species, and biomass constituent analyses for the biomass feedstock. The observed relatively high mass ratio of volatile matter to fixed carbon (5.18), coupled with the high content of holocellulose, could favor the porosity development of intermediate pyrolytic char and derived carbons. On the other hand, the reasonably low ash content (i.e., below 5%) is crucial to minimize the negative effect of inorganic species, which might occupy some sodium storage active sites and trigger side reactions during sodiation.[30] However, the presence of both K and Ca (the most abundant species in WHH ash) can be interesting, since it is widely accepted that they play a key role in promoting devolatilization as well as secondary charring reactions,[31] leading to morphological and structural changes in the resulting HCs. In conclusion, the properties of WHH seem to be appropriate for the purpose of this study.

Table 1. Summarized Properties of Raw WHH Samples Used in the Present Study

proximate analysis (wt %)		lignocellulosic constituents and extractives (wt % in dry basis)	
moisture	9.24 ± 0.56	hemicellulose	38.1 ± 1.84
volatile matter (dry basis)	81.3 ± 1.96	cellulose	32.0 ± 3.36
fixed carbon (dry basis)	15.7 ± 0.88	lignin	23.8 ± 1.66
ash (dry basis)	3.00 ± 0.33	extractives	3.10 ± 0.23
ultimate analysis (wt % in dry ash-free basis)		**main inorganic species detected by ICP-MS (g kg^{-1} dry WHH)**	
C	46.3 ± 0.21	K	14.0
H	5.70 ± 0.13	Ca	10.8
N	0.50 ± 0.04	Al	10.4
O (by difference)	44.5	Mg	1.70
		P	1.40
		Si	1.02
		Na	0.40

Properties of WHH-Derived Hard Carbons. Mass yields of the produced HCs (in dry basis, with respect to raw WHH) ranged from 8.8 to 15%, depending on the severity of the activation process. From Figures S2b and S3—which show SEM images of the raw WHH, WHH-derived char, and two chemically activated carbons (HP-700-1 and HP-800-1)—it can be seen that the resulting char after the pyrolysis step at 500 °C retained the fiber-shaped morphology of the raw WHH (with fibers of ∼10 μm diameter). This morphology was still maintained after chemical activation. However, HC-800-1 exhibited more distinguishable macropores as a consequence of the higher extent of K_2CO_3 decomposition and subsequent release of gas species at 800 °C.

For their part, the HRTEM images and the corresponding fast Fourier transform (FTT) patterns shown in Figures 2 and S4 provided valuable insights into the nanostructural features of HCs. A highly amorphous structure can be observed for both WHH-derived char and HC-700-1, with highly disordered and curled carbon layers (see Figure S4a,b). Nevertheless, considerable thinner carbon sheets with large randomly oriented ordered domains (and relatively short interlayer distances) were observed for HC-700-4 (see Figure 2a,b). For HCs carbonized at 800 °C, however, a mostly disordered structure with locally ordered domains having

https://doi.org/10.1021/acs.energyfuels.3c01040
Energy Fuels 2023, 37, 9650−9661

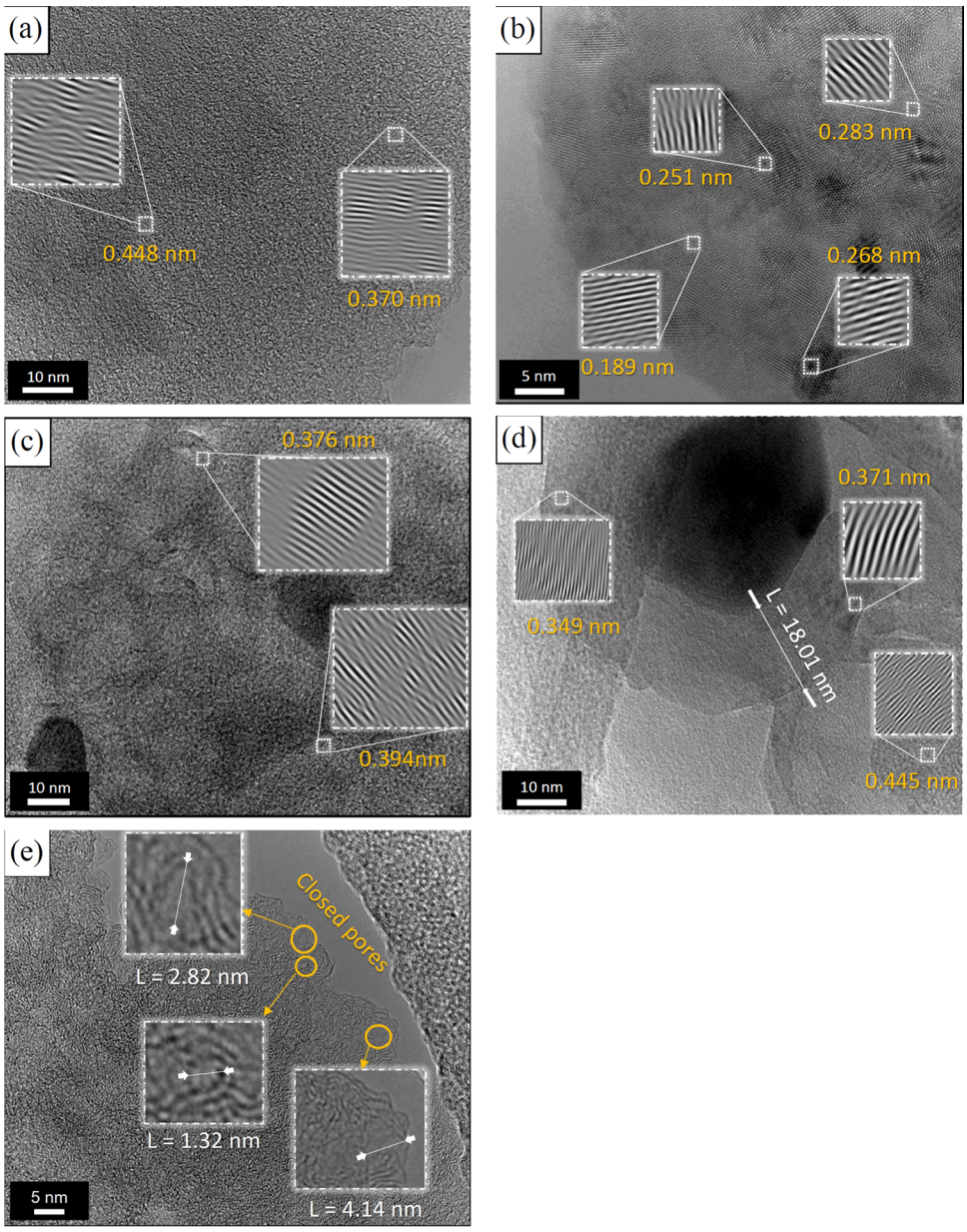

Figure 2. HRTEM micrographs of HC-700-4 (a, b), HHC-800-1 (c), and HHC-800-4 (d, e). Insets (squares) show enlarged views of micrographs to enhance visualization of the lattice fringes.

relatively large interplanar distances (up to 0.445 nm) was observed (see Figure 2c,d). This tendency is consistent with the FFT patterns shown in Figure S4, where the sharpest diffraction rings were visible for HCs annealed at 700 °C. Furthermore, Figure 2d clearly shows that highly ordered microdomains were located around pores for HC-800-4; this could be explained by deposition of recondensed/repolymerized volatiles and/or a higher extent of catalytic graphitization by locally available metallic potassium.[32,33] HC-800-4 also exhibited a certain number of small closed pores, as shown in Figure 2e. This finding was a bit unexpected since much higher annealing temperatures (typically above 1000 °C) are required for developing closed porosity.[34]

Figure 3a displays the XRD spectra obtained for the WHH-derived HCs. As expected, two wide peaks centered at ca. 23 and 44° were observed, corresponding to (002) and (100 and 101) planes for graphitic crystallites within turbostratic structures.[35] From the interplanar spacing between graphene layers (d_{002}), apparent crystallite thickness along the *c*-axis (L_c), and apparent crystallite width along the *a*-axis (L_a) values reported in Table 2 and calculated using the Bragg's and Scherrer's equations,[36] some considerations can be made. First, the interplanar spacing was considerably greater than that of graphite (0.335 nm) for all of the carbons synthesized in the present study, indicating an a priori favorable scenario for Na-ion storage.[37,38] Second, the trend observed for L_a values seems to be consistent with the aforementioned HRTEM results, since smaller values were estimated for HC-800-4 (more disordered) in comparison with the HCs prepared at lower impregnation ratios and/or lower annealing temperatures.

With regard to Raman spectroscopy results, Figure 3b,c shows the decomposed spectra for HC-700-4 and HC-800-4 (see also Figure S5 for the rest of the HCs), assuming one Gaussian-shaped band (D3) and four Lorentzian-shaped bands

https://doi.org/10.1021/acs.energyfuels.3c01040
Energy Fuels 2023, 37, 9650−9661

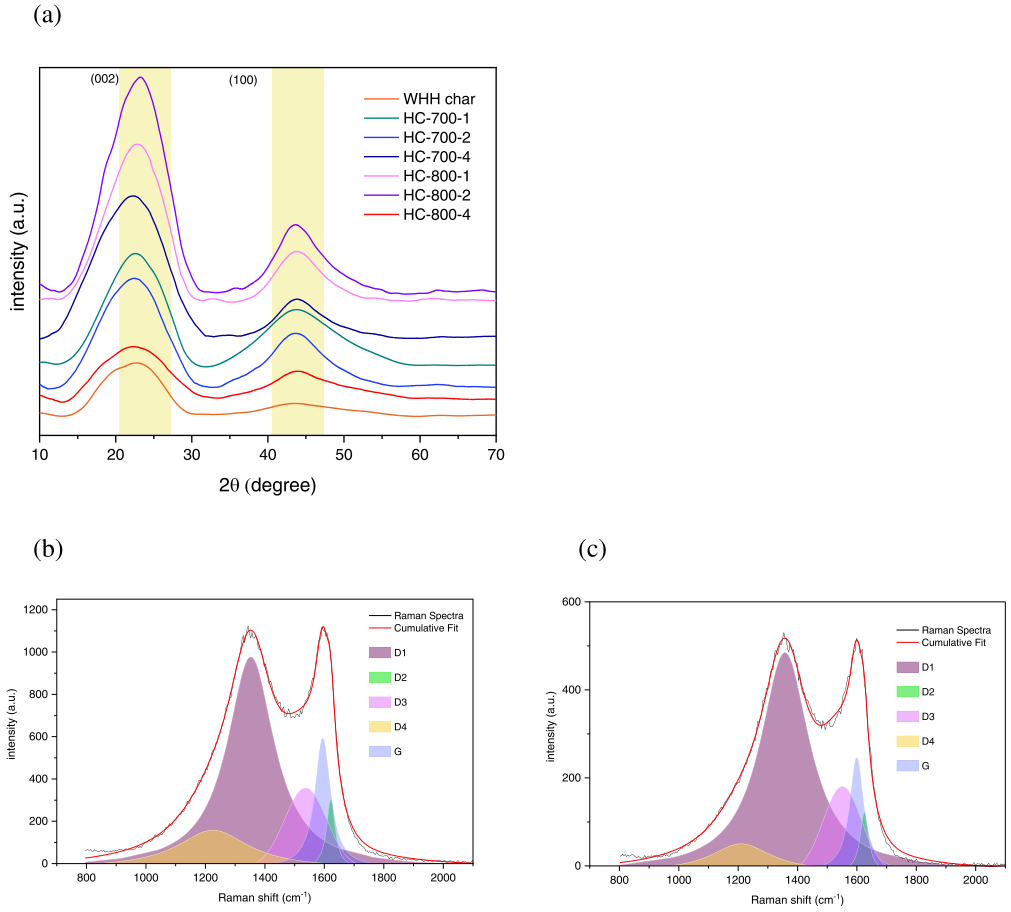

Figure 3. XRD patterns of WHH-derived carbons (a) and Raman spectra of HC-700-4 (b) and HC-800-4 (c).

Table 2. Structural Features of WHH-Derived HCs from XRD and Raman Analyses

material	d_{002} (nm)	L_a (nm)	L_c (nm)	A_{D1}/A_G	A_{D3}/A_G
HC-700-1	0.396	1.544	0.962	2.77 ± 0.128	0.829 ± 0.061
HC-700-2	0.402	1.889	0.894	4.01 ± 0.342	0.986 ± 0.087
HC-700-4	0.397	2.347	0.806	4.09 ± 0.547	1.08 ± 0.14
HC-800-1	0.395	2.497	0.969	3.85 ± 1.01	1.11 ± 0.16
HC-800-2	0.389	2.319	0.948	3.91 ± 1.18	0.767 ± 0.064
HC-800-4	0.397	1.598	0.883	6.17 ± 0.432	1.28 ± 0.087

Table 3. XPS Peak Assignments and Area Percentages for C 1s and N 1s regions[43−45] (Deconvoluted C 1s and N 1s Spectra for Selected Carbons are Given in Figures S6 and S7)

	C 1s			N 1s		
material	peak 1 (285.0 eV), C−C, C═C, C_{sp^2}−N	peak 2 (285.8−286.7 eV), C−O, C═O, C_{sp^3}−N	peak 3 (288.4−289.1 eV), O−C═O, C bonded to heteroatoms	peak 1 (398.8−399.1 eV), pyridinic N	peak 2 (400.0−401.0 eV), pyrrolic + pyridine N	peak 3 (401.1−401.3 eV), graphitic N
WHH char	82	10	8	18	82	
HC-700-1	71	22	7	40	60	
HC-700-2	58	26	16	17	83	
HC-700-4	61	31	8	10	90	
HC-800-1	66	24	10	26		74
HC-800-2	72	15	13	23		77
HC-800-4	59	29	12	33		67

(G, D1, D2, and D4).[39] These bands are consensually attributed to disordered graphitic lattices (D1, D2, and D4), amorphous carbon (D3), and graphitic sp^2 bonding (G). Curve fitting was performed using the Pick Analyzer tool in OriginPro software. The resulting A_{D1}/A_G and A_{D3}/A_G area ratios, which are commonly used to characterize the degree of disorder of biomass chars,[40−42] are also listed in Table 2. From the values of both area ratios, it can be deduced that the higher

https://doi.org/10.1021/acs.energyfuels.3c01040
Energy Fuels 2023, 37, 9650−9661

Table 4. Textural Features Deduced from N_2 and CO_2 Adsorption Isotherms Given in Figure S8

material	S_{BET}[a] (m^2 g^{-1})	S_{BET}[b] (m^2 g^{-1})	micropore volume[c] (cm^3 g^{-1})	mesopore volume[c] (cm^3 g^{-1})	ultramicropore volume[d] (cm^3 g^{-1})
WHH char	159.8	107.5	0.0668	0.0205	0.0323
HC-700-1	205.2	151.2	0.0679	0.0366	0.0281
HC-700-2	207.8	176.1	0.0947	0.0015	0.0308
HC-700-4	266.0	179.8	0.1156	0.0067	0.0298
HC-800-1	26.23	157.6	0.0213	0.0003	0.0273
HC-800-2	65.80	151.2	0.0331	0.0094	0.0246
HC-800-4	333.5	192.3	0.1408	0.0095	0.0372

[a]From N_2 adsorption isotherm. [b]From CO_2 adsorption isotherm. [c]From N_2 adsorption data using a NLDFT model. [d]From CO_2 adsorption data using a NLDFT model.

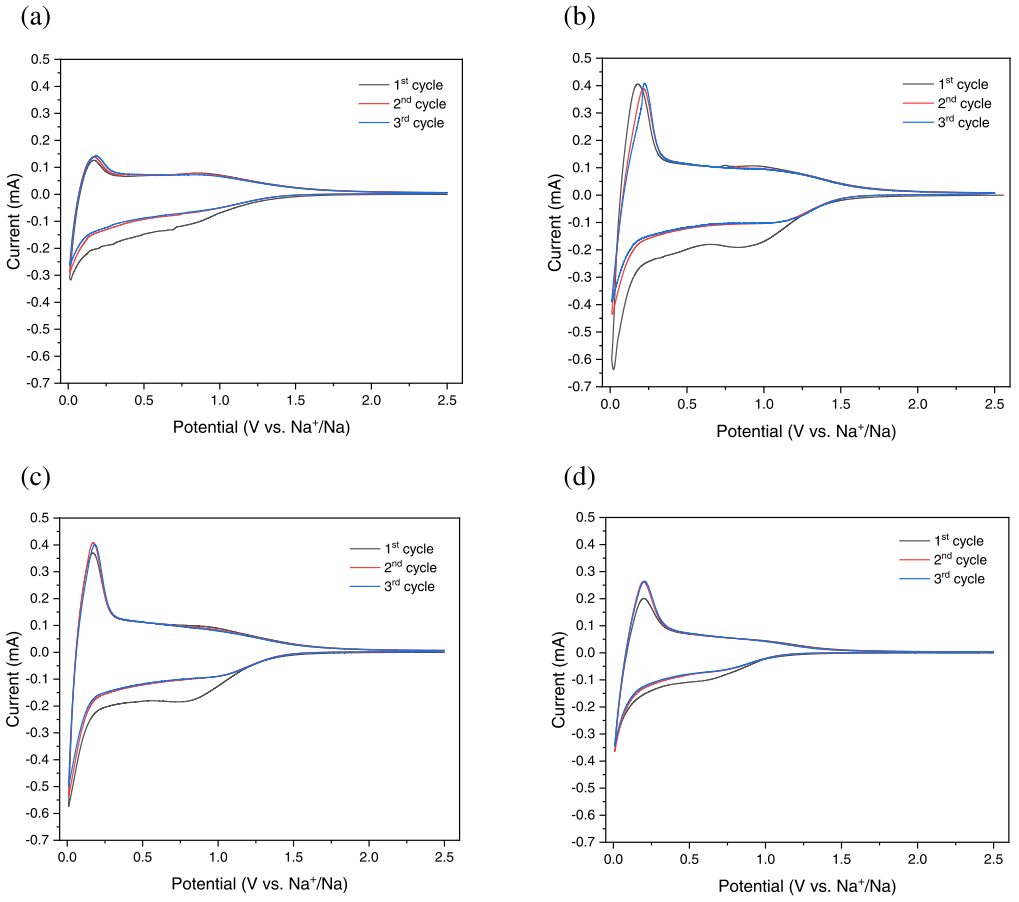

Figure 4. CV curves obtained using two-electrode setups for the first three cycles of HC-700-1 (a), HC-700-4 (b), HC-800-1 (c), and HC-800-4 (d).

the impregnation ratio at a given temperature, the higher the degree of disorder. At 800 °C, a marked increase in both A_{D1}/A_G and A_{D3}/A_G area ratios was observed when the highest impregnation ratio was used. Hence, the information extracted from Raman spectra was qualitatively consistent with the findings deduced from HRTEM and XRD data.

From Table 3, which summarizes the data obtained from XPS measurements and deconvolutions of C 1s and N 1s regions (see Figures S6 and S7, respectively), it can be seen that K_2CO_3 activation led to a marked increase in the availability of oxygen-containing surface groups, even when HCs were produced at 800 °C. This is consistent with the trend observed for the oxygen content measured by EDX (see Table S1). Regarding the N-containing groups, pyrrolic N (N-5) was converted into more stable quaternary (graphitic) N when the highest carbonization temperature increased up to 800 °C. In the case of HC-800-4, the observed slightly lower proportion of quaternary N (compared to that of HC-800-1 and HC-800-2) could be ascribed to its higher degree of structural disorder. It could be hypothesized that K-catalyzed etching reaction between CO_2 and the carbon matrix leads to a slight increase in the amount of edge N.

Concerning the textural properties, Table 4 reports the results obtained from the N_2 and CO_2 adsorption isotherms shown in Figure S8. As can be seen, K_2CO_3 activation did not result in a marked increase in porosity. The largest BET specific surface areas (335.5 and 192.3 m^2 g^{-1} from N_2 and CO_2 adsorption, respectively), which were obtained for the carbon produced under the more severe activation conditions (HC-800-4), were considerably lower than those reported in the literature; for instance, Xi et al. reported a surface area of 2300 m^2 g^{-1} for K_2CO_3-activated waste lignin-derived

https://doi.org/10.1021/acs.energyfuels.3c01040
Energy Fuels 2023, 37, 9650−9661

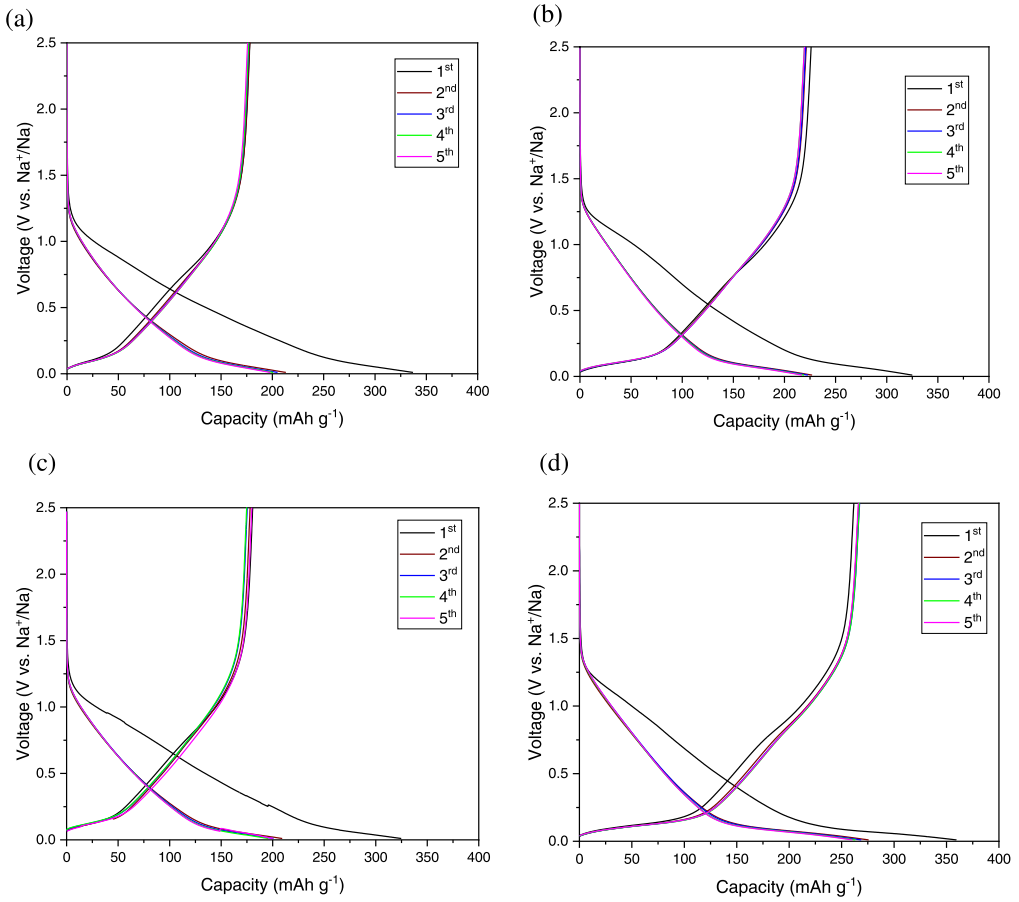

Figure 5. GCD curves obtained using two-electrode half-cells for the first five cycles (0.03 A g^{-1}) of HC-700-1 (a), HC-700-4 (b), HC-800-1 (c), and HC-800-4 (d).

carbons.[32] The mild activation that has been achieved in the present study can be explained by the fact that the slurry obtained after wet impregnation was filtered, leading to chars with far lower contents of activating agent than expected. With regard to the pore size distributions (obtained from both adsorbates assuming a NLDFT-based model) shown in Figures S9 and S10, the following considerations can be made: (1) activation did not result in any increase in the volume of mesopores, quite the contrary, with the exception of HC-700-1; (2) the volume of ultramicropores hardly changed with respect to that of the WHH-derived char; and (3) most of the new porosity observed for HC-700-4 and HC-800-4 was in the form of micropores with widths comprised between 0.7 and 1.0 nm.

Electrochemical Performance. The acquired CV curves (for the first three discharge−charge cycles) are shown in Figure 4. The two characteristic peaks appearing at ca. 0.01 V (cathodic) and 0.15−0.25 V (anodic) can be mainly ascribed to the reversible insertion/extraction of Na ions, respectively.[46] On the other hand, the broad cathodic peak observed at 0.25−1.25 V for all of the carbons during the first discharge can be attributed to SEI formation as well as to irreversible adsorption of Na ions on high binding energy sites (e.g., structural defects and surface functional groups).[47] Interestingly, the area of this irreversible peak was considerably lower for HC-800-4, despite its higher surface area. This finding is in agreement with the previous study by Zheng et al.,[1] who stated that porous carbons having a developed narrow microporosity—as is the case of HC-800-4—did not result in a thicker SEI, since the electrolyte solvent and the anion will probably be unable to diffuse into and wet the narrow micropores (i.e., below 1 nm). Furthermore, the almost overlapped CV profiles obtained for the second and third cycles confirmed the stability of the formed SEI layer.

The first five galvanostatic discharge−charge cycles at a current density of 0.03 A g^{-1} for the selected carbons using two-electrode half-cells are shown in Figure 5 (see also Figure S11 for the rest of the HCs). As expected, all of the profiles showed a slope region (from 2.5 to ca. 0.15 V) and a plateau region (from ca. 0.15 to 0.01 V). According to the current state of knowledge, the slope region could mainly be ascribed to adsorption of Na ions on the surface and at defects, whereas the second one is commonly associated to slower filling processes (of graphitic interlayers and closed pores).[48] In the case of the WHH-derived char, the plateau region was negligible (see Figure S11a), largely due to its poor conductivity caused by an excessively low degree of graphitization. Among all of the tested HCs, HC-800-4 exhibited the best sodium storage performance at 0.03 A g^{-1}, with first discharge and charge capacities of 359.5 and 261.7 mAh g^{-1}, respectively. In consonance with the CV results, this material exhibited the highest ICE (73%). The better performance of HC-800-4 in terms of reversible capacity is due to the large plateau contribution, suggesting that this carbon possesses more Na-ion storage sites with low binding energies. In this sense, the closed pores observed for HC-800-4 (see Figure 2e) can be accessible to Na ions, which can then fill them at very low voltages.[34] The developed narrow micro-

https://doi.org/10.1021/acs.energyfuels.3c01040
Energy Fuels 2023, 37, 9650−9661

porosity observed for this HC, coupled with large enough interplanar distances between graphene layers, can provide effective diffusion pathways, allowing Na ions to reach these closed pores.

To assess the rate capability of HC-based working electrodes, five discharge−charge cycles at different current densities were performed using two-electrode half-cells. As clearly shown in Figure 6, HC-800-4 was always the best-performing material regardless of the current density applied, exhibiting reversible charging capacities of 267, 240, 204, 102, and 79 mAh g^{-1} when cycled at 0.03, 0.06, 0.1, 0.5 and 1 A g^{-1}; respectively (see all measured charge capacities per unit mass and per unit area in Tables S2 and S3, respectively). Although better rate capabilities have already been reported in the literature for biomass-derived HCs,[11,49−57] it should be noted that more severe operating conditions (i.e., higher carbonization temperatures and/or more corrosive chemical agents) were adopted for producing the active materials. In addition, and as highlighted in Table 5, all of these previous studies reported ICE values considerably lower than that of the best-performing HC reported here (73%).

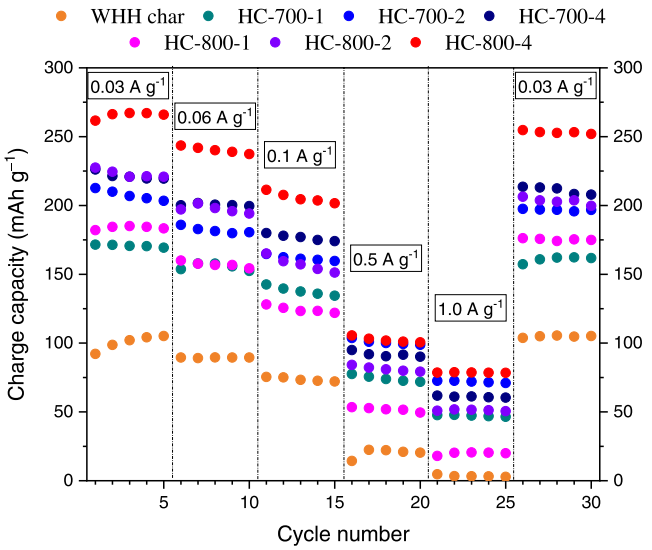

Figure 6. Charge specific capacities at various current densities ranging from 0.03 to 1 A g^{-1} (two-electrode setup).

From Figure 6, it can also be seen that as the current density returned to 0.03 A g^{-1}, the charge specific capacities were very similar to those measured during the first five cycles. In particular, HC-800-4 recovered 95% of its initial capacity (253 mAh g^{-1} vs 267 mAh g^{-1}), indicating a good stability of the electrode when relatively high current rates were applied.

Since it is well known that using two-electrode half-cell setups can lead to discharge capacity underestimation, due to additional overpotentials introduced by the metallic sodium CE,[36] the rate capability test was repeated for HC-800-4 using a three-electrode half-cell (see Figure S1a). As shown in Figure S12, the use of a two-electrode cell resulted in a considerable underestimation of capacity, especially at relatively low current rates. However, at 0.5 and 1 A g^{-1}, the measured discharge capacities only differed by 3−4%. The three-electrode setup was used for measuring the cycling stability of HC-800-4 over 300 cycles at a high current density of 2 A g^{-1}. Figure 7a displays the resulting charge capacities, which were of ca. 50 mAh g^{-1} at this high current rate. After 300 cycles at 2 A g^{-1}, when the current rate was set to its initial value (0.03 A g^{-1}), 96% of the initial reversible capacity was retained, confirming the excellent cycling stability of the electrode.

Figure 7b,c and Tables S4−S7 show the apparent diffusion coefficients (D_{Na^+}) deduced from GITT measurements (at 0.03 A g^{-1}) for sodiation and desodiation processes, respectively (see the Supporting Information for more details). The WE was previously subjected to three CV scans at 0.1 mV s^{-1} to allow the formation and stabilization of the SEI. From Figure 7b, different sodiation mechanisms can be identified along the voltage profile. The relatively fast first stage taking place above 0.1 V could mainly be ascribed to adsorption of Na ions on the surface and at structural defects. For its part, the decrease in D_{Na^+} values at voltages below 0.1 V could probably be linked to slower intercalation (into graphene interlayers) and pore filling processes. Moreover, the overcoming of the repulsive forces

Table 5. Electrochemical Performance of Several Biomass-Derived HCs—as Anodes in SIBs—Reported in the Literature

precursor	HC synthesis	reversible capacity (mAh g^{-1}) at current density (A g^{-1})	ICE (%)	capacity retention (%)	ref
corn stalk	carbonization at 1200 °C followed by dual N−P doping	143 at 1; 122 at 2	53	91 (after 2000 cycles at 1 A g^{-1})	49
apple waste	activation with H_3PO_4 and subsequent carbonization at 1100 °C	112 at 1; 86 at 2	61	100 (after 1000 cycles at 1 A g^{-1})	50
pistachio shells	hydrothermal pretreatment with NaOH at 165 °C for 6 h and subsequent carbonization at 1000 °C	95 at 1.2; 56 at 3	62	100 (after 500 cycles at 0.4 A g^{-1})	51
pomelo peels	chemical activation via H_3PO_4 impregnation and further heating at 700 °C	118 at 1; 94.5 at 2	27	85 (after 230 cycles at 0.05 A g^{-1})	11
coffee grounds	chemical activation via KOH impregnation and further heating at 900 °C	141 at 1	52	92 (after 200 cycles at 1 A g^{-1})	52
orange peels	chemical activation via KOH impregnation and further heating at 800 °C	125 at 1	42	94 (after 100 cycles at 1 A g^{-1})	53
peanut shells	chemical activation via H_3PO_4 impregnation and further heating at 800 °C	140 at 1; 110 at 2	56	81 (after 120 at 0.02 A g^{-1})	54
peanut shells	hydrothermal pretreatment with NaOH at 165 °C for 4 h and subsequent carbonization at 800 °C	100 at 1.5	58	97 (after 100 cycles at 0.02 A g^{-1})	55
peanut shells	chemical activation via KOH impregnation and further heating at 600 °C	150 at 1	33	86 (after 3000 cycles at 1 A g^{-1})	56
peanut skin	hydrothermal pretreatment with H_2SO_4 at 180 °C for 24 h and subsequent activation with KOH impregnation and further heating at 800 °C	154 at 1; 47 at 10	33	43 (after 200 cycles at 0.5 A g^{-1})	57

https://doi.org/10.1021/acs.energyfuels.3c01040
Energy Fuels 2023, 37, 9650−9661

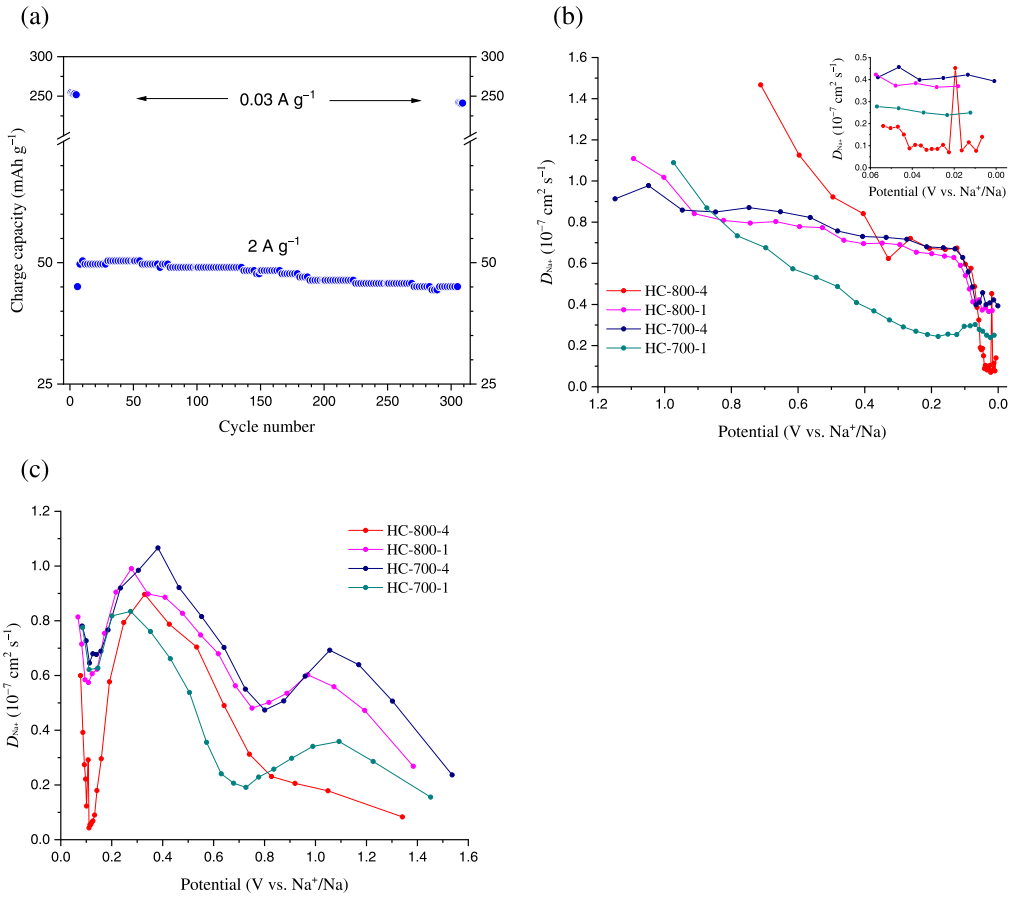

Figure 7. Cycling performance of HC-800-4 over 300 cycles at 2 A g^{-1} (a), D_{Na^+} values estimated from GITT measurements (for selected HCs) during sodiation (b) and desodiation (c).

arising from the interactions between Na ions and the surface of the electrode to diffuse into the microcrystalline phase can also explain the observe decrease in the apparent diffusion coefficients.[58] In the case of HC-800-4, the sudden increase in D_{Na^+} at ca. 0.02 V could be attributed to the fact that certain Na ions reached the closed micropores available in this material, as revealed by the HRTEM image given in Figure 2e. With regard to the desodiation process (see Figure 7c), the marked negative peak observed for HC-800-4 at ca. 0.1 V is consistent with the considerations made for the opposite process and could indicate that the Na ions trapped into the closed pores did not reach sufficient diffusion paths for their fast desorption. In addition, the positive peak observed for HC-700-1, HC-700-4, and HC-800-1 at 0.9−1.1 V—probably related to desorption of Na ions from surface functional groups—was not observed for HC-800-4. This could suggest that the slope region for this more disordered carbon material could be more attributed to adsorption of Na ions at structural defects rather than on surface functional groups.

CONCLUSIONS

To sum up, the findings of the preset study indicate that hard carbons produced from waste hump hurd via mild chemical activation with K_2CO_3 at 800 °C exhibit remarkable electrochemical performance as anodes in SIBs. The balance attained for HC-800-4 in terms of material features, which is translated into a moderate interconnected microporosity (with pore sizes below 1 nm), an appropriate concentration of defects in the carbon structure—coupled with the presence of pseudographitic domains having large interplanar distances—and a certain number of closed pores, can explain the observed relatively high capacity at high current rates. In comparison with other hard carbon-based anodes synthesized via more energy-intense, expensive, and/or difficult to scale-up processes, the best-performing WHH-derived carbon reported herein represents a very interesting starting-point candidate for two main reasons: (1) the possibility to easily scale up the production process to industrially relevant capacities, and (2) its relatively high ICE. Further research on improving its specific capacity at industrially relevant current densities—through, for instance, heteroatom doping and encapsulation of redox-active nanoparticles—without compromising, or ever increasing, the ICE will be crucial to definitely establish the potential of waste hemp-hurd-derived hard carbons.

ASSOCIATED CONTENT

Supporting Information

The Supporting Information is available free of charge at https://pubs.acs.org/doi/10.1021/acs.energyfuels.3c01040.

Schematic of the electrochemical cells used; additional data from characterization of materials (SEM and HRTEM images, Raman and XPS spectra, elemental composition, adsorption isotherms, and pore sizes distributions); additional GCD curves; specific charge capacities (using two- and three-electrode setup); and values of the apparent diffusion coefficients (PDF)

https://doi.org/10.1021/acs.energyfuels.3c01040
Energy Fuels 2023, 37, 9650−9661

AUTHOR INFORMATION

Corresponding Author

Joan J. Manyà − *Aragón Institute of Engineering Research (I3A), Thermochemical Processes Group, University of Zaragoza, 22071 Huesca, Spain; Department of Chemical Engineering and Environmental Technologies, University of Zaragoza, 50018 Zaragoza, Spain;* orcid.org/0000-0002-0118-3254; Email: joanjoma@unizar.es

Authors

Daniel Antorán − *Aragón Institute of Engineering Research (I3A), Thermochemical Processes Group, University of Zaragoza, 22071 Huesca, Spain; Department of Chemical Engineering and Environmental Technologies, University of Zaragoza, 50018 Zaragoza, Spain*

Darío Alvira − *Aragón Institute of Engineering Research (I3A), Thermochemical Processes Group, University of Zaragoza, 22071 Huesca, Spain; Department of Chemical Engineering and Environmental Technologies, University of Zaragoza, 50018 Zaragoza, Spain;* orcid.org/0000-0002-5526-3962

M. Eser Peker − *Faculty of Science, Department of Chemistry, Ege University, 35100 Izmir, Turkey*

Hugo Malón − *Department of Mechanical Engineering, University of Zaragoza, 22071 Huesca, Spain*

Silvia Irusta − *Department of Chemical Engineering and Environmental Technologies, University of Zaragoza, 50018 Zaragoza, Spain; Aragón Institute of Nanoscience and Materials (INMA), CSIC—University of Zaragoza, 50018 Zaragoza, Spain; Networking Research Center on Bioengineering, Biomaterials and Nanomedicine, CIBER-BBN, 28029 Madrid, Spain;* orcid.org/0000-0002-2966-9088

Víctor Sebastián − *Department of Chemical Engineering and Environmental Technologies, University of Zaragoza, 50018 Zaragoza, Spain; Aragón Institute of Nanoscience and Materials (INMA), CSIC—University of Zaragoza, 50018 Zaragoza, Spain; Networking Research Center on Bioengineering, Biomaterials and Nanomedicine, CIBER-BBN, 28029 Madrid, Spain;* orcid.org/0000-0002-6873-5244

Complete contact information is available at: https://pubs.acs.org/10.1021/acs.energyfuels.3c01040

Notes

The authors declare no competing financial interest.

ACKNOWLEDGMENTS

This work is part of the research project PID2019-107737RB-I00, funded by MCIN/AEI/10.13039/501100011033. The authors acknowledge the funding from the Aragon Government (ref T22_20R). D. Alvira also acknowledges the funding from the Aragon Government with a grant for postgraduate research contracts (2019−2023). LMA-ELECMI and NANBIOSIS ICTs are gratefully acknowledged.

ABBREVIATIONS

NLDFT = non-local density functional theory
SEM-EDX = scanning electron microscopy coupled with energy dispersive X-ray spectroscopy
HRTEM = high-resolution transmission electron microscopy
XRD = X-ray diffraction
XPS = X-ray photoelectron spectroscopy

REFERENCES

(1) Zheng, Y.; Lu, Y.; Qi, X.; Wang, Y.; Mu, L.; Li, Y.; Ma, Q.; Li, J.; Hu, Y. S. Superior electrochemical performance of sodium-ion full-cell using poplar wood derived hard carbon anode. *Energy Storage Mater.* **2019**, *18*, 269−279.

(2) Martin, G.; Rentsch, L.; Höck, M.; Bertau, M. Lithium market research − global supply, future demand and price development. *Energy Storage Mater.* **2017**, *6*, 171−179.

(3) Zhou, X.; Wan, L.-J.; Guo, Y.-G. Binding SnO2 Nanocrystals in Nitrogen-Doped Graphene Sheets as Anode Materials for Lithium-Ion Batteries. *Adv. Mater.* **2013**, *25*, 2152−2157.

(4) Dunn, B.; Kamath, H.; Tarascon, J. M. Electrical energy storage for the grid: A battery of choices. *Science* **2011**, *334*, 928−935.

(5) Sun, J.; Xu, Y.; Lv, Y.; Zhang, Q.; Zhou, X. Recent Advances in Covalent Organic Framework Electrode Materials for Alkali Metal-Ion Batteries. *CCS Chem.* **2023**, *5*, 1259−1276.

(6) Kim, H.; Hong, J.; Yoon, G.; Kim, H.; Park, K. Y.; Park, M. S.; Yoon, W. S.; Kang, K. Sodium intercalation chemistry in graphite. *Energy Environ. Sci.* **2015**, *8*, 2963−2969.

(7) Huang, J.; Zhang, W.; Yu, P.; Dong, H.; Zheng, M.; Xiao, Y.; Hu, H.; Liu, Y.; Liang, Y. Direct carbonization of black liquor powders into 3D honeycomb-like porous carbons with a tunable disordered degree for sodium-ion batteries. *New J. Chem.* **2020**, *44*, 10697−10702.

(8) Xu, T.; Qiu, X.; Zhang, X.; Xia, Y. Regulation of surface oxygen functional groups and pore structure of bamboo-derived hard carbon for enhanced sodium storage performance. *Chem. Eng. J.* **2023**, *452*, No. 139514.

(9) Karatrantos, A.; Cai, Q. Effects of pore size and surface charge on Na ion storage in carbon nanopores. *Phys. Chem. Chem. Phys.* **2016**, *18*, 30761−30769.

(10) Li, W.; Huang, J.; Feng, L.; Cao, L.; Ren, Y.; Li, R.; Xu, Z.; Li, J.; Yao, C. Controlled synthesis of macroscopic three-dimensional hollow reticulate hard carbon as long-life anode materials for Na-ion batteries. *J. Alloys Compd.* **2017**, *716*, 210−219.

(11) Hong, K.-l.; Qie, L.; Zeng, R.; Yi, Z.; Zhang, W.; Wang, D.; Yin, W.; Wu, C.; Fan, Q.; Zhang, W.; Huang, Y. h. Biomass derived hard carbon used as a high performance anode material for sodium ion batteries. *J. Mater. Chem. A* **2014**, *2*, 12733.

(12) Di Stasi, C.; Greco, G.; Canevesi, R. L. S.; Izquierdo, M. T.; Fierro, V.; Celzard, A.; González, B.; Manyà, J. J. Influence of activation conditions on textural properties and performance of activated biochars for pyrolysis vapors upgrading. *Fuel* **2020**, *289*, No. 119759.

(13) Hayashi, J.; Horikawa, T.; Takeda, I.; Muroyama, K.; Nasir Ani, F. Preparing activated carbon from various nutshells by chemical activation with K2CO3. *Carbon* **2002**, *40*, 2381−2386.

(14) Wei, H.; Chen, J.; Fu, N.; Chen, H.; Lin, H.; Han, S. Biomass-derived nitrogen-doped porous carbon with superior capacitive performance and high CO2 capture capacity. *Electrochim. Acta* **2018**, *266*, 161−169.

(15) Li, S.; Han, K.; Li, J.; Li, M.; Lu, C. Preparation and characterization of super activated carbon produced from gulfweed by KOH activation. *Microporous Mesoporous Mater.* **2017**, *243*, 291−300.

(16) Sevilla, M.; Ferrero, G. A.; Fuertes, A. B. Beyond KOH activation for the synthesis of superactivated carbons from hydrochar. *Carbon* **2017**, *114*, 50−58.

(17) Fechler, N.; Fellinger, T. P.; Antonietti, M. "salt templating": A simple and sustainable pathway toward highly porous functional carbons from ionic liquids. *Adv. Mater.* **2013**, *25*, 75−79.

(18) Wang, L.; Rao, L.; Xia, B.; Wang, L.; Yue, L.; Liang, Y.; DaCosta, H.; Hu, X. Highly efficient CO2 adsorption by nitrogen-doped porous carbons synthesized with low-temperature sodium amide activation. *Carbon* **2018**, *130*, 31−40.

(19) Hayashi, J.; Horikawa, T.; Muroyama, K.; Gomes, V. G. Activated carbon from chickpea husk by chemical activation with

K2CO3: Preparation and characterization. *Microporous Mesoporous Mater.* **2002**, *55*, 63−68.
(20) Adinata, D.; Wan Daud, W. M. A.; Aroua, M. K. Preparation and characterization of activated carbon from palm shell by chemical activation with K2CO3. *Bioresour. Technol.* **2007**, *98*, 145−149.
(21) Carvalho, A.; Gomes, M.; Mestre, A.; Pires, J.; Brotas de Carvalho, M. Activated carbons from cork waste by chemical activation with K2CO3. *Carbon* **2004**, *42*, 672−674.
(22) Carrott, P. J. M.; Ribeiro Carrott, M. M. L.; Mourão, P. A. M. Pore size control in activated carbons obtained by pyrolysis under different conditions of chemically impregnated cork. *J. Anal. Appl. Pyrolysis* **2006**, *75*, 120−127.
(23) European Commission. Hemp Production on the EU. https://agriculture.ec.europa.eu/farming/crop-productions-and-plant-based-products/hemp_en (accessed January 27, 2023).
(24) Um, J. H.; Ahn, C. Y.; Kim, J.; Jeong, M.; Sung, Y. E.; Cho, Y. H.; Kim, S. S.; Yoon, W. S. From grass to battery anode: Agricultural biomass hemp-derived carbon for lithium storage. *RSC Adv.* **2018**, *8*, 32231−32240.
(25) Wang, H.; Xu, Z.; Kohandehghan, A.; Li, Z.; Cui, K.; Tan, X.; Stephenson, T. J.; King'ondu, C. K.; Holt, C. M. B.; Olsen, B. C.; et al. Interconnected Carbon Nanosheets Derived from Hemp for Ultrafast Supercapacitors with High Energy. *ACS Nano* **2013**, *7*, 5131−5141.
(26) Wang, P.; Zhu, K.; Ye, K.; Gong, Z.; Liu, R.; Cheng, K.; Wang, G.; Yan, J.; Cao, D. Three-dimensional biomass derived hard carbon with reconstructed surface as a free-standing anode for sodium-ion batteries. *J. Colloid Interface Sci.* **2020**, *561*, 203−210.
(27) Rodríguez-Correa, C.; Hehr, T.; Voglhuber-Slavinsky, A.; Rauscher, Y.; Kruse, A. Pyrolysis vs. hydrothermal carbonization: Understanding the effect of biomass structural components and inorganic compounds on the char properties. *J. Anal. Appl. Pyrolysis* **2019**, *140*, 137−147.
(28) Greco, G.; Videgain, M.; Di Stasi, C.; González, B.; Manyà, J. J. Evolution of the mass-loss rate during atmospheric and pressurized slow pyrolysis of wheat straw in a bench-scale reactor. *J. Anal. Appl. Pyrolysis* **2018**, *136*, 18−26.
(29) Greco, G.; Di Stasi, C.; Rego, F.; González, B.; Manyà, J. J. Effects of slow-pyrolysis conditions on the products yields and properties and on exergy efficiency: A comprehensive assessment for wheat straw. *Appl. Energy* **2020**, *279*, No. 115842.
(30) Zhang, T.; Mao, J.; Liu, X.; Xuan, M.; Bi, K.; Zhang, X. L.; Hu, J.; Fan, J.; Chen, S.; Shao, G. Pinecone biomass-derived hard carbon anodes for high-performance sodium-ion batteries. *RSC Adv.* **2017**, *7*, 41504−41511.
(31) Manyà, J. J.; Alvira, D.; Azuara, M.; Bernin, D.; Hedin, N. Effects of Pressure and the Addition of a Rejected Material from Municipal Waste Composting on the Pyrolysis of Two-Phase Olive Mill Waste. *Energy Fuels* **2016**, *30*, 8055−8064.
(32) Xi, Y.; Wang, Y.; Yang, D.; zhang, Z.; Liu, W.; Li, Q.; Qiu, X. K2CO3 activation enhancing the graphitization of porous lignin carbon derived from enzymatic hydrolysis lignin for high performance lithium-ion storage. *J. Alloys Compd.* **2019**, *785*, 706−714.
(33) Govind Raj, K.; Joy, P. A. Role of localized graphitization on the electrical and magnetic properties of activated carbon. *J. Am. Ceram. Soc.* **2017**, *100*, 5151−5161.
(34) Au, H.; Alptekin, H.; Jensen, A. C. S.; Olsson, E.; O'Keefe, C. A.; Smith, T.; Crespo-Ribadeneyra, M.; Headen, T. F.; Grey, C. P.; Cai, Q.; et al. A revised mechanistic model for sodium insertion in hard carbons. *Energy Environ. Sci.* **2020**, *13*, 3469−3479.
(35) Ramirez, N.; Sardella, F.; Deiana, C.; Schlosser, A.; Müller, D.; Kißling, P. A.; Klepzig, L. F.; Bigall, N. C. Capacitive behavior of activated carbons obtained from coffee husk. *RSC Adv.* **2020**, *10*, 38097−38106.
(36) Alvira, D.; Antorán, D.; Manyà, J. J. Assembly and electrochemical testing of renewable carbon-based anodes in SIBs: A practical guide. *J. Energy Chem.* **2022**, *75*, 457−477.
(37) Väli, R.; Jänes, A.; Thomberg, T.; Lust, E. Synthesis and characterization of D-glucose derived nanospheric hard carbon negative electrodes for lithium- and sodium-ion batteries. *Electrochim. Acta* **2017**, *253*, 536−544.
(38) Cao, L.; Hui, W.; Xu, Z.; Huang, J.; Zheng, P.; Li, J.; Sun, Q. Rape seed shuck derived-lamellar hard carbon as anodes for sodium-ion batteries. *J. Alloys Compd.* **2017**, *695*, 632−637.
(39) Sadezky, A.; Muckenhuber, H.; Grothe, H.; Niessner, R.; Pöschl, U. Raman microspectroscopy of soot and related carbonaceous materials: Spectral analysis and structural information. *Carbon* **2005**, *43*, 1731−1742.
(40) Wang, X.; Chen, Q.; Zhu, H.; Chen, X.; Yu, G. In-situ study on structure evolution and gasification reactivity of biomass char with K and Ca catalysts at carbon dioxide atmosphere. *Carbon Resour. Convers.* **2023**, *6*, 27−33.
(41) Yu, J.; Guo, Q.; Ding, L.; Gong, Y.; Yu, G. Studying effects of solid structure evolution on gasification reactivity of coal chars by in-situ Raman spectroscopy. *Fuel* **2020**, *270*, No. 117603.
(42) Mubari, P. K.; Beguerie, T.; Monthioux, M.; Weiss-Hortala, E.; Nzihou, A.; Puech, P. The X-ray, Raman and TEM Signatures of Cellulose-Derived Carbons Explained. *C* **2022**, *8*, No. 4.
(43) Singh, B.; Fang, Y.; Cowie, B. C. C.; Thomsen, L. NEXAFS and XPS characterisation of carbon functional groups of fresh and aged biochars. *Org. Geochem.* **2014**, *77*, 1−10.
(44) Ayiania, M.; Smith, M.; Hensley, A. J. R.; Scudiero, L.; McEwen, J. S.; Garcia-Perez, M. Deconvoluting the XPS spectra for nitrogen-doped chars: An analysis from first principles. *Carbon* **2020**, *162*, 528−544.
(45) Deng, X.; Li, J.; Shan, Z.; Sha, J.; Ma, L.; Zhao, N. A N, O co-doped hierarchical carbon cathode for high-performance Zn-ion hybrid supercapacitors with enhanced pseudocapacitance. *J. Mater. Chem. A* **2020**, *8*, 11617−11625.
(46) Alvin, S.; Yoon, D.; Chandra, C.; Cahyadi, H. S.; Park, J. H.; Chang, W.; Chung, K. Y.; Kim, J. Revealing sodium ion storage mechanism in hard carbon. *Carbon* **2019**, *145*, 67−81.
(47) Wahid, M.; Gawli, Y.; Puthusseri, D.; Kumar, A.; Shelke, M. V.; Ogale, S. Nutty Carbon: Morphology Replicating Hard Carbon from Walnut Shell for Na Ion Battery Anode. *ACS Omega* **2017**, *2*, 3601−3609.
(48) Alvira, D.; Antorán, D.; Manyà, J. J. Plant-derived hard carbon as anode for sodium-ion batteries: A comprehensive review to guide interdisciplinary research. *Chem. Eng. J.* **2022**, *447*, No. 137468.
(49) Qin, D.; Liu, Z.; Zhao, Y.; Xu, G.; Zhang, F.; Zhang, X. A sustainable route from corn stalks to N, P-dual doping carbon sheets toward high performance sodium-ion batteries anode. *Carbon* **2018**, *130*, 664−671.
(50) Wu, L.; Buchholz, D.; Vaalma, C.; Giffin, G. A.; Passerini, S. Apple-Biowaste-Derived Hard Carbon as a Powerful Anode Material for Na-Ion Batteries. *ChemElectroChem* **2016**, *3*, 292−298.
(51) Xu, S.-D.; Zhao, Y.; Liu, S.; Ren, X.; Chen, L.; Shi, W.; Wang, X.; Zhang, D. Curly hard carbon derived from pistachio shells as high-performance anode materials for sodium-ion batteries. *J. Mater. Sci.* **2018**, *53*, 12334−12351.
(52) Chiang, P. H.; Liu, S. F.; Hung, Y. H.; Tseng, H.; Guo, C. H.; Chen, H. Y. Coffee-Ground-Derived Nanoporous Carbon Anodes for Sodium-Ion Batteries with High Rate Performance and Cyclic Stability. *Energy Fuels* **2020**, *34*, 7666−7675.
(53) Xiang, J.; Lv, W.; Mu, C.; Zhao, J.; Wang, B. Activated hard carbon from orange peel for lithium/sodium ion battery anode with long cycle life. *J. Alloys Compd.* **2017**, *701*, 870−874.
(54) Dou, X.; Hasa, I.; Saurel, D.; Jauregui, M.; Buchholz, D.; Rojo, T.; Passerini, S. Impact of the Acid Treatment on Lignocellulosic Biomass Hard Carbon for Sodium-Ion Battery Anodes. *ChemSusChem* **2018**, *11*, 3276−3285.
(55) Ren, X.; Xu, S. D.; Liu, S.; Chen, L.; Zhang, D.; Qiu, L. Lath-shaped biomass derived hard carbon as anode materials with super rate capability for sodium-ion batteries. *J. Electroanal. Chem.* **2019**, *841*, 63−72.
(56) Lv, W.; Wen, F.; Xiang, J.; Zhao, J.; Li, L.; Wang, L.; Liu, Z.; Tian, Y. Peanut shell derived hard carbon as ultralong cycling anodes

https://doi.org/10.1021/acs.energyfuels.3c01040
Energy Fuels 2023, 37, 9650−9661

for lithium and sodium batteries. *Electrochim. Acta* **2015**, *176*, 533−541.
(57) Wang, H.; Yu, W.; Shi, J.; Mao, N.; Chen, S.; Liu, W. Biomass derived hierarchical porous carbons as high-performance anodes for sodium-ion batteries. *Electrochim. Acta* **2016**, *188*, 103−110.
(58) Darjazi, H.; Bottoni, L.; Moazami, H. R.; Rezvani, S. J.; Balducci, L.; Sbrascini, L.; Staffolani, A.; Tombesi, A.; Nobili, F. From waste to resources: transforming olive leaves to hard carbon as sustainable and versatile electrode material for Li/Na-ion batteries and supercapacitors. *Mater. Today Sustainability* **2023**, *21*, No. 100313.

https://doi.org/10.1021/acs.energyfuels.3c01040
Energy Fuels 2023, 37, 9650−9661